

# Collective suppression of optical hyperfine pumping in dense clouds of atoms in microtraps

Shimon Machluf,<sup>1</sup> Julian B. Naber,<sup>1</sup> Maarten L. Soudijn,<sup>1</sup> Janne Ruostekoski,<sup>2</sup> and Robert J. C. Spreeuw<sup>1</sup>

<sup>1</sup>*Van der Waals-Zeeman Institute, Institute of Physics, University of Amsterdam, Science Park 904, 1098XH Amsterdam, The Netherlands*

<sup>2</sup>*Department of Physics, Lancaster University, Lancaster, LA1 4YB, United Kingdom*

We observe a density-dependent collective suppression of optical pumping between the hyperfine ground states in an array of submicrometer-sized clouds of cold rubidium atoms. The suppressed Raman transition rate can be explained by strong resonant dipole-dipole interactions that are enhanced by increasing atom density. The observations are consistent with stochastic electrodynamics simulations that incorporate the effects of the nonlinear population transfer via internal atomic levels embedded in a coupled-dipole model.

Interfaces between trapped atoms and light play a central role, e.g., in sensing [1], metrology [2], nonlinear devices [3, 4], and quantum information processing [5]. For example, trapped cold atomic ensembles are utilized in the development of quantum memories, quantum repeaters, and as an interface to convert between flying and standing qubits [6–12]. For many quantum information protocols, such as those based on Rydberg interaction [13, 14], it is also essential to confine the atoms in lattices [15–18]. A typical length scale of Rydberg dipole-dipole interaction is around  $5\ \mu\text{m}$ , necessitating a comparable size lattice spacing. Engineering smaller lattice periods attract interest as a route towards interaction between atoms and nanostructured surfaces [19] or increased tunneling rates of atoms between adjacent sites [20–24]. For example, in order to increase the hopping energy above the cloud temperature one would benefit from lattice spacings well below the optical wavelength [25].

Understanding the fundamental properties of the interaction of resonant light with trapped atomic ensembles is essential for all of the above applications, and has consequently attracted considerable recent experimental interest [26–36]. The observed phenomena in atomic systems include suppression of light scattering in small samples [27], subradiance [31], superflash effects [29], and the dependence of the response on the quantum statistics [32]. Several established models of the resonance response in continuous medium electrodynamics may be violated in cold and dense atomic ensembles [34, 35, 37, 38]. This is because each atom is subject to the driving field plus the fields scattered by the other atoms. These fields mediate strong resonant dipole-dipole interactions between the atoms, resulting in collective excitations whose behavior cannot be described as a sum of the responses of isolated atoms.

Most experiments on the collective optical responses of cold atoms are performed either in dilute ensembles or in the limit of low light intensity which can be analyzed on the assumption that each atom responds to light as a simple damped linear harmonic oscillator. Here we ex-

tend both the experiment and theory beyond the limit of low light intensity where optical pumping becomes relevant. This corresponds to a situation in many applications of atom-light interfaces. For example, the optical protocols for quantum memories commonly use a spontaneous Raman scattering event to store a single photon as a collective spin wave in the ensemble [6].

Here we report on the suppression of optical pumping between hyperfine levels, due to resonant dipole-dipole interactions in magnetically trapped submicron clouds. Our results reveal strongly density-dependent behavior, originating from collectively suppressed spontaneous Raman transitions. We perform our measurements in a two-dimensional  $10\ \mu\text{m}$  period lattice of magnetic microtraps on an atom chip [39, 40]. The technology of microtraps provides a natural platform with cold-atom-light interfaces at high atom densities and large optical cross-sections [41]. This allows us to reach a strong collective coupling between atoms and light in a structured and engineered environment where high atom densities can be achieved. The large array of atom traps provides us with parallel measurements over a large range of initial densities that are simultaneously obtained at each run of the experiment.

In the experiment, optical pumping is performed between hyperfine ground states of dense rubidium ensembles and measured by detecting the remaining atoms in the initial state. We find that the transition rate is suppressed as the density increases. In the numerical simulations the optical pumping process necessitates stochastic electrodynamics simulations that incorporate the population transfer between internal levels of the atoms, and we implement a recently proposed model of coupled many-atom internal level dynamics [42]. This is different from most experiments that are performed in the limit of low light intensity and therefore can be analyzed by standard coupled-dipole model simulations with each atom responding to light as a (simple) damped linear harmonic oscillator. Similarly to the experiment, the simulations reveal a density-dependent suppression of optical pumping that is shown to result from the collective response;

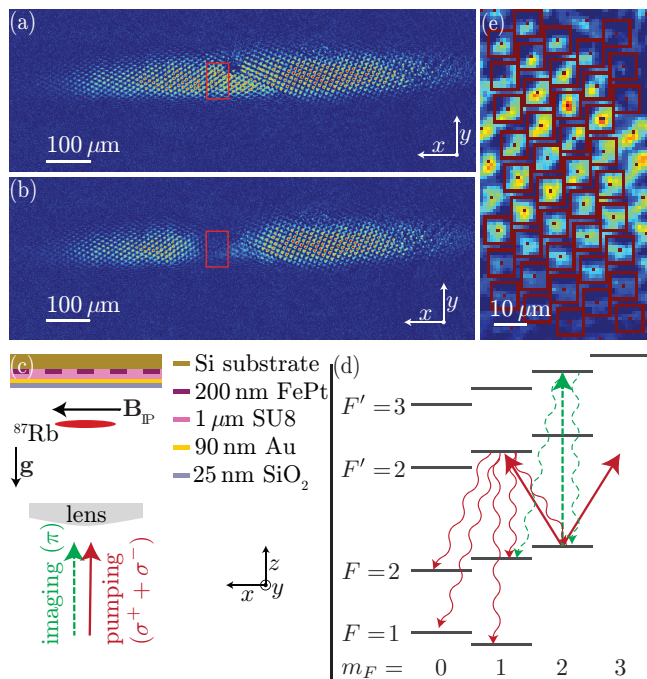


FIG. 1. Description of the apparatus. (a) A sample image after the macroscopic cloud is loaded into the lattice of the microtraps. The false color indicates the integrated atomic density along the imaging axis (optical density), which is proportional to the number of atoms in each microtrap. (b) Similar image to (a) but after the depletion laser is pulsed for a long time ( $> 100 \mu\text{s}$ ). The area where this laser impinges on the atoms is visible as depleted microtraps. (c) A sketch of the apparatus showing the atom chip (with its different layers), the macroscopic cloud below the atom chip, the lens used for imaging, and the two relevant lasers: pumping and imaging. (d) A sketch of the relevant atomic levels (hyperfine structure and Zeeman sublevel). The straight arrows show the first possible excitation, assuming the atoms are in the  $|2, 2\rangle$  state, and the wavy arrows show the possible decay channels. The reabsorbed photons have many more absorption and emission paths, which are not shown. (e) A magnification of the area marked by the red rectangle in (a) showing the individual microtraps. Each trap's center is marked with a dot, and the squares mark the area where atoms are counted and considered to belong to one microtrap.

the Raman transition rate between the internal levels in an interacting atomic ensemble is suppressed as compared with the rate of independent atoms. The origin of the suppression is strong resonant dipole-dipole interactions between the atoms. We also identify a collective transition resonance that is blue-shifted as the atom density is increased.

The apparatus is described in [40]. Briefly, we have an atom chip where the trapping potential is generated by a patterned layer of permanent magnet (FePt) film. Together with a homogeneous magnetic field a lattice of Ioffe-Pritchard type microtraps is created  $\sim 8 \mu\text{m}$  from the surface. The lattice can have different ge-

ometries, and in this atom chip we have triangular and square lattices with  $10 \mu\text{m}$  periodicity (the experiment here was done on the triangular lattice). We load  $^{87}\text{Rb}$  atoms in the  $(5S_{1/2}) |F, m_F\rangle = |2, 2\rangle$  ground-state and with temperature of  $\sim 15 \mu\text{K}$  into the microtraps [see Fig. 1(a) for a sample image] with calculated averaged trapping frequency of  $2\pi \times 14 \text{ kHz}$  [(7,18,22) kHz in the  $(x, y, z)$  directions]. The calculated trap size (root-mean-square of the density) is  $\sigma_{x,y,z} = (0.86, 0.34, 0.27) \mu\text{m} = (6.9, 2.7, 2.2) 1/k$ , and the peak atomic density is  $\rho = 8 \times 10^{11} \text{ N/cm}^3 = 0.0015 \text{ N} \times k^3$ , where  $N$  is the number of atoms in the microtrap and  $k = 2\pi/\lambda$  ( $\lambda$  is the transition wavelength). In order to calculate the number of atoms from the optical density image we use an absorption cross section based on optical Bloch equations (OBE) simulation of optical Zeeman pumping during the  $\pi$  polarized probe pulse. We also remove noise from the image using a fringe removal algorithm and deconvolute the image with an experimentally measured point-spread-function [43].

After the loading we wait  $\sim 20 \text{ ms}$  for untrapped atoms to leave the microtraps area. We then pulse a focused laser beam ( $\sim 100 \mu\text{m}$  waist) with detuning  $\Delta = \Omega - \omega$  (the laser and atomic transition frequencies, respectively) from the  $(5P_{3/2}) F' = 2$  transition [44] for a varying length of pumping time  $t_p$ , causing atom loss due to decay to untrappable or dark states [Fig. 1(b)]. This pumping laser has  $\sigma^+ + \sigma^-$  polarization and a power of  $\approx 0.15 \text{ mW/cm}^2$ , which results in saturation parameter of  $s \approx 0.02$  for the pumping laser transition. After the pulse we image the remaining atoms in the  $F = 2$  ground-state using absorption imaging with  $\pi$  polarized light to the  $F' = 3$  state, see Fig. 1(c,d) for a sketch of the apparatus and the generated transitions. The analysis of the images [43] is done on a region marked with the red rectangle in Fig. 1(a,b), and magnified in Fig. 1(e).

In order to lower the experimental noise, we group the microtraps into 9 groups based on their initial number of atoms [43]. These groups are the basis for the analysis below. The difference in initial population is due to the Gaussian shape of the original macroscopic cloud, and since the microtraps are identical, the density is proportional to the number of trapped atoms.

As the pumping time  $t_p$  is increased, the atoms are pumped to dark or untrappable states, and the number of atoms in the initial state decays. Figure 2 shows this decay for different initial atom numbers, each curve representing a different group of microtraps. In addition, we see a change of the slope after  $t_p \approx 15 \mu\text{s}$  (more clearly visible in the inset), hence we fit the data to two exponents,  $N_{1,2}^0 \exp(-\gamma_{1,2}t)$ , where the 1, 2 indices are used for  $t_p \leq 15 \mu\text{s}$  and  $t_p > 15 \mu\text{s}$ , respectively. It is important to note that the transition between the two exponents occurs at a fixed time, rather than at a fixed density. This indicates that the second exponent is an effect of our measurement procedure and may be due to light-induced dipolar forces and collisions that were also

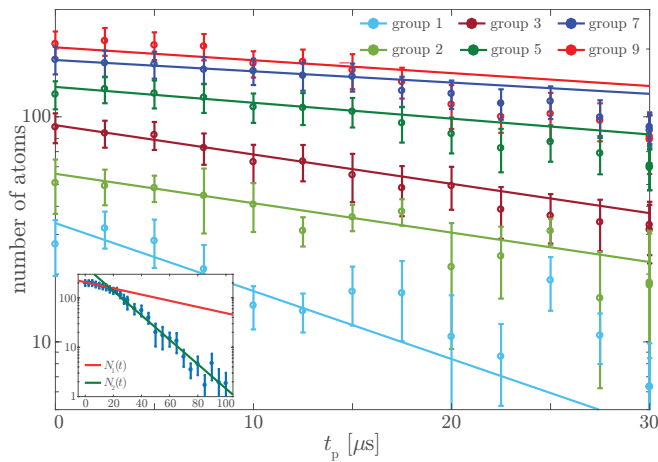


FIG. 2. Number of atoms as a function of pumping times ( $\Delta = 0$ ) in a semilog plot for different groups of microtraps, representing different initial densities. Initial density increases from group 1 (lower curve) to group 9 (upper curve), and for clarity not all nine groups are shown). The first  $15 \mu\text{s}$  of each data set are fitted to an exponent, and the fitted slope is suppressed as the density increases. At longer depletion times the decay rate is different, and another exponent is used. These second exponents are not shown in the main figure. The inset shows an example of data (from group 8) for longer depletion times, where the two-exponent behavior is visible. The errorbars are root-mean-square of the statistical error due to repetitions and different microtraps within each group, and the error of the calculated absorption cross section.

shown to lead to enhanced losses for longer laser pulses in Ref. [27]. Additional contributions could be, for example, from pumping effects in our multilevel system (total of 8 ground-state Zeeman sublevels) and the finite life-time of the untrapped Zeeman sublevels, which is  $\sim 10 - 15 \mu\text{s}$  and is limited by thermal velocity and trap size.

Figure 3(a) shows the fitted decay rates,  $\gamma_{1,2}$ , as a function of the pumping laser detuning, forming a Lorentzian shape transition rate, with fitted maximum decay rates  $\gamma_{1,2}^{\text{max}}$ . Figure 3(b) summarizes the results for the different groups (i.e., different initial densities) of microtraps. The amplitudes of the fitted Lorentzians are shown for  $t_p \leq 15 \mu\text{s}$  ( $\gamma_1^{\text{max}}$ ) and for  $t_p > 15 \mu\text{s}$  ( $\gamma_2^{\text{max}}$ ). A dependence on the density of atoms is visible only for short times, i.e. in  $\gamma_1^{\text{max}}$ . To within our signal-to-noise level, we do not observe any density-dependence of the Lorentzian width or center frequency.

The density-dependent suppression of the pumping rate  $\gamma_1^{\text{max}}$  constitutes the central result of the paper. It cannot be explained by standard OBE but results from the collective response of the atoms, generated by the strong resonant dipole-dipole interactions. We find that significant suppression starts at surprisingly low atom densities of  $\rho/k^3 \lesssim 0.1$ , which is especially relevant for the operation of quantum devices [1–3, 7, 8, 12, 13] and protocols [14, 21–24] that rely on the interaction between

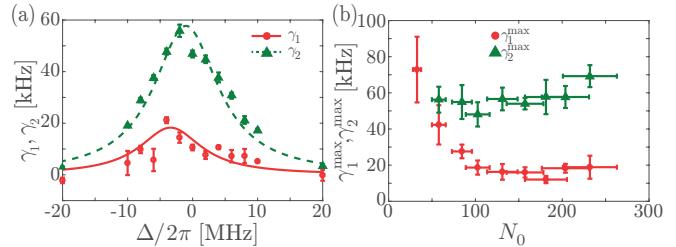


FIG. 3. (a) The decay rate of the two exponents is plotted for different detuning, and two Lorentzians are fitted to the data (here taken from group 8). The Lorentzian that fits the data of the first  $15 \mu\text{s}$  is clearly suppressed (i.e., has lower amplitude) compared to the data taken at longer times. (b) Density-dependent suppression of the decay rate. The maximum decay rate [ $\gamma_{1,2}^{\text{max}}$  in (a)] is plotted as a function of the averaged initial number of atoms  $N_0$  of each group. In the least populated traps, group 1, the data point of the second exponent is absent due to low number of atoms that is below our noise level.

light and trapped atoms. For example, communication protocols [6] are based on spontaneous Raman scattering, and as the atomic systems become smaller and denser, this rate will be suppressed.

Along with the experimental observations we performed stochastic electrodynamics simulations that further confirm the collective density-dependent suppression of the optical pumping. In the coupled-dipole model simulations [45] the electrodynamics of radiatively coupled atoms is solved for stochastically sampled atomic positions from the density distribution. Ensemble-averaging over many such realizations then yields the optical response. The stochastic treatment of atomic coordinates establishes the position-dependent correlations between the atoms that go beyond the standard mean-field theory of continuous medium electrodynamics [38]. In the limit of low light intensity the coupled-dipole model simulations for stationary (cold) atoms with a simple level structure are exact [42]. Here we extend the standard coupled-dipole model beyond the limit of low light intensity using a recently proposed model [42] of internal atomic level dynamics that incorporates the effects of the nonlinear population transfer. We do this by introducing a semi-classical approximation that neglects the quantum entanglement between the internal electronic levels and allows significantly larger atom numbers than full quantum treatments [46]. Closely related semi-classical approaches have also been introduced in Refs. [47, 48].

The formalism is explained in detail in [43]. In each stochastic realization of  $N$  atomic positions  $\{\mathbf{X}_1, \dots, \mathbf{X}_N\}$ , we write a single particle density matrix  $\hat{\rho}_{ab}(\mathbf{r})$  for the different electronic sublevels  $a, b$  as the sum over the atoms  $j$ ,  $\langle \hat{\rho}_{ab}(\mathbf{r}) \rangle_{\{\mathbf{x}_1, \dots, \mathbf{x}_N\}} = \sum_j \rho_{ab}^{(j)} \delta(\mathbf{r} - \mathbf{X}_j)$ . Instead of considering the full experimental configuration

of all the  $F = 1, 2$  and  $F' = 2$  electronic levels, we approximate the system by an effective three-level model where one of the ground levels refers to the initial state  $|1\rangle \equiv |2, 2\rangle$ , and all the final electronic ground levels are approximated by a single state  $|2\rangle$ . Resonant incident light then drives the transition  $|1\rangle \leftrightarrow |e\rangle$  to an electronically excited state  $|e\rangle$ , and the atoms can spontaneously decay to both levels  $|1\rangle$  and  $|2\rangle$ . For the equal transition strengths for the two levels, a set of coupled equations of motion for internal level one-body density matrix elements  $\rho_{ab}^{(j)}$  ( $a, b = 1, 2, e$ ), for each atom  $j = 1, \dots, N$  then take a simple form. For example,

$$\begin{aligned} \frac{d}{dt} \rho_{11}^{(j)} = & +\Gamma \rho_{ee}^{(j)} + \sqrt{2} \text{Im} \left[ \frac{\xi}{\mathcal{D}} \rho_{e1}^{(j)} \hat{\mathbf{e}}_1^* \cdot \mathbf{D}_F^+(\mathbf{X}_j) \right] \\ & + \text{Im} \left[ \xi \sum_{l \neq j} \mathcal{G}_{1g}^{(jl)} \rho_{ge}^{(l)} \rho_{e1}^{(j)} \right]. \end{aligned} \quad (1)$$

Here the summations run over the  $N$  atoms and the ground levels  $g = 1, 2$ ;  $\mathcal{D}$  is the reduced dipole matrix element,  $\xi = \mathcal{D}^2 / (\hbar \epsilon_0)$ ,  $\hat{\mathbf{e}}_1$  is the unit vector along the direction of the dipole matrix element for the  $|1\rangle \leftrightarrow |e\rangle$  transition, and  $\Gamma$  denotes the Wigner-Weisskopf resonance linewidth. We treat the positive frequency component of the slowly-varying incident light field  $\mathbf{D}_F^+$  as a plane wave. The last term in Eq. (9e) describes the light-mediated interactions between the atoms  $j$  and  $l$ , where  $\mathcal{G}_{gg'}^{(jl)}$  denotes the dipole radiation propagator for light that is radiated from the  $g' \leftrightarrow e$  transition of the atom  $l$  to the  $g \leftrightarrow e$  transition of the atom  $j$  [43]. In the absence of the coupling terms  $\mathcal{G}_{gg'}^{(jl)}$ , the equations reduce to OBE. The terms  $\mathcal{G}_{gg'}^{(jl)}$  represent the strong resonant dipole-dipole interactions that depend on the relative positions between the atoms and lead to spatial correlations in the optical response.

The suppression of the pumping rate in the simulations [43] due to collective dipole-dipole interactions is illustrated in Fig. 4 for different atom numbers and trap sizes. The  $N = 1$  result represents the solution that is obtained by solving OBE for the pumping, therefore the suppressed pumping rates per atom for the higher densities are a direct consequence of the collective resonance dipole-dipole interactions between the atoms. Although simulations using the experimental numbers of atoms are not feasible, we find qualitatively similar behavior due to the collective density-dependent effects. Moreover, the numerics reveal that the suppression strongly depends on density, but it is also affected by the sample size; e.g., for the same density the smaller traps are less suppressed. See Fig. 4(b) for results of various trap volumes.

The measurements of the resonance shifts in the spectroscopy of dense atom samples have attracted considerable attention recently [30, 33–36], and especially the origin of the shifts (or the absence of them) has been actively studied [34–38]. Although we were not able to resolve

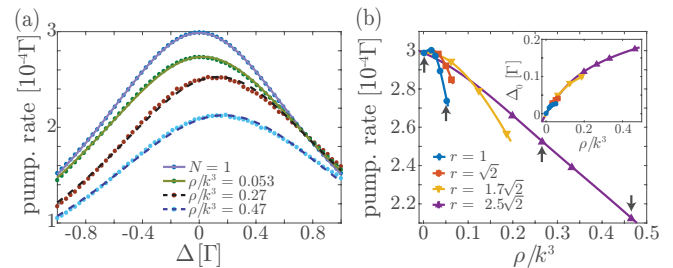


FIG. 4. Stochastic simulation results for the optical pumping of atoms in a three-level system when the atoms are interacting via light-induced resonant dipole-dipole interactions with  $s = 0.01$ . (a) The spectrum of the pumping rate per atom as a function of the detuning of light from the single-atom resonance for different initial densities (increasing density from top to bottom). The dots are simulation results, and the lines are fits to Lorentzians. The collective dipole-dipole interactions lead to density-dependent suppression of the pumping rate. The solid lines are fits to results of simulations of a trap with the same size and aspect ratio as the experimental traps, and the dashed lines are for simulated traps with volume smaller by a ratio  $r^3 = (2.5\sqrt{2})^3$ . (b) The fitted amplitudes and resonance shifts (inset) of Lorentzians as in (a) for different densities and trap volumes. The simulations for the different traps are performed for up to  $N = 35, 15, 9, 7$  atoms (for  $r = 1, \sqrt{2}, 1.7\sqrt{2}, 2.5\sqrt{2}$ , respectively) [43]. The solid lines are interpolations of the simulation results, and the  $N = 1$  solution was added to all trap volumes. The points marked with arrows are the fitted amplitudes of the four data-sets shown in (a).

them experimentally, the simulation results in Fig. 4(a) [and summarised in the inset in Fig. 4(b)] show a blue-shifted collective resonance as the density is increased. For the calculated cases, the density-dependence of the shift is no longer linear. Moreover, it is about an order of magnitude less than the Lorentz-Lorenz shift and has the opposite sign, consistently with the recent transmission measurements [36]. Interestingly, we also find that the shift is larger for smaller traps at the same density, indicating dependence on the system size.

To conclude, we show experimentally and theoretically that optical pumping is suppressed in small, dense clouds due to collective resonant dipole-dipole interactions. This suppression is already significant at densities of  $\rho/k^3 \lesssim 0.1$ . In addition, the simulations show a collective transition resonance that is blue-shifted as the atom density is increased.

We thank C. Adams, T. Pfau, and M. D. Lee for stimulating discussions. Our work is financially supported by the Netherlands Organization for Scientific Research (NWO) and EPSRC. JBN acknowledges financial support by the Marie Curie program ITN-Coherence (265031).

- [1] Dmitry Budker and Michael Romalis, “Optical magnetometry,” *Nature Physics* **3**, 227 (2007).
- [2] Andrew D. Ludlow, Martin M. Boyd, Jun Ye, E. Peik, and P. O. Schmidt, “Optical atomic clocks,” *Rev. Mod. Phys.* **87**, 637–701 (2015).
- [3] S. E. Harris, “Electromagnetically induced transparency,” *Physics Today* **50**, 36–42 (1997).
- [4] M. Fleischhauer, A. Imamoglu, and J. P. Marangos, “Electromagnetically induced transparency: Optics in coherent media,” *Rev. Mod. Phys.* **77**, 633–673 (2005).
- [5] Klemens Hammerer, Anders S. Sørensen, and Eugene S. Polzik, “Quantum interface between light and atomic ensembles,” *Rev. Mod. Phys.* **82**, 1041–1093 (2010).
- [6] L. M. Duan, M. D. Lukin, J. I. Cirac, and P. Zoller, “Long-distance quantum communication with atomic ensembles and linear optics,” *Nature* **414**, 413–418 (2001).
- [7] D. N. Matsukevich and A. Kuzmich, “Quantum State Transfer Between Matter and Light,” *Science* **306**, 663–666 (2004), <http://science.sciencemag.org/content/306/5696/663.full.pdf>.
- [8] C. H. van der Wal, M. D. Eisaman, A. André, R. L. Walsworth, D. F. Phillips, A. S. Zibrov, and M. D. Lukin, “Atomic Memory for Correlated Photon States,” *Science* **301**, 196+ (2003).
- [9] T. Chanelière, D. N. Matsukevich, S. D. Jenkins, S.-Y. Lan, T. A. B. Kennedy, and A. Kuzmich, “Storage and retrieval of single photons transmitted between remote quantum memories,” *Nature* **438**, 833 (2005).
- [10] C. W. Chou, H. de Riedmatten, D. Felinto, S. V. Polyakov, S. J. van Enk, and H. J. Kimble, “Measurement-induced entanglement for excitation stored in remote atomic ensembles,” *438*, 828–832 (2005).
- [11] Chin-Wen Chou, Julien Laurat, Hui Deng, Kyung S. Choi, Hugues de Riedmatten, Daniel Felinto, and H. Jeff Kimble, “Functional Quantum Nodes for Entanglement Distribution over Scalable Quantum Networks,” *Science* **316**, 1316+ (2007).
- [12] Zhen-Sheng Yuan, Yu-Ao Chen, Bo Zhao, Shuai Chen, Jorg Schmiedmayer, and Jian-Wei Pan, “Experimental demonstration of a BDCZ quantum repeater node,” *454*, 1098–1101 (2008).
- [13] M. Saffman, T. G. Walker, and K. Mølmer, “Quantum information with Rydberg atoms,” *Rev. Mod. Phys.* **82**, 2313–2363 (2010).
- [14] Y. O. Dudin, L. Li, F. Bariani, and A. Kuzmich, “Observation of coherent many-body Rabi oscillations,” *Nat Phys* **8**, 790–794 (2012).
- [15] P. Schauß, J. Zeiher, T. Fukuhara, S. Hild, M. Cheneau, T. Macrì, T. Pohl, I. Bloch, and C. Gross, “Crystallization in Ising quantum magnets,” *Science* **347**, 1455–1458 (2015), <http://science.sciencemag.org/content/347/6229/1455.full.pdf>.
- [16] Manuel Endres, Hannes Bernien, Alexander Keesling, Harry Levine, Eric R. Anschuetz, Alexandre Krajenbrink, Crystal Senko, Vladan Vuletic, Markus Greiner, and Mikhail D. Lukin, “Atom-by-atom assembly of defect-free one-dimensional cold atom arrays,” *Science* **354**, 1024–1027 (2016), <http://science.sciencemag.org/content/354/6315/1024.full.pdf>.
- [17] Daniel Barredo, Sylvain de Léséleuc, Vincent Lienhard, Thierry Lahaye, and Antoine Browaeys, “An atom-by-atom assembler of defect-free arbitrary two-dimensional atomic arrays,” *Science* **354**, 1021–1023 (2016), <http://science.sciencemag.org/content/354/6315/1021.full.pdf>.
- [18] Johannes Zeiher, Rick van Bijnen, Peter Schauß, Sebastian Hild, Jae-yoon Choi, Thomas Pohl, Immanuel Bloch, and Christian Gross, “Many-body interferometry of a Rydberg-dressed spin lattice,” *Nature Physics* **12**, 1095 EP – (2016).
- [19] J. D. Thompson, T. G. Tiecke, N. P. de Leon, J. Feist, A. V. Akimov, M. Gullans, A. S. Zibrov, V. Vuletić, and M. D. Lukin, “Coupling a Single Trapped Atom to a Nanoscale Optical Cavity,” *Science* **340**, 1202–1205 (2013).
- [20] Immanuel Bloch, “Ultracold quantum gases in optical lattices,” *Nat Phys* **1**, 23–30 (2005).
- [21] V. Y. F. Leung, A. Tauschinsky, N. J. Druten, and R. J. C. Spreeuw, “Microtrap arrays on magnetic film atom chips for quantum information science,” *Quantum Information Processing, Quantum Information Processing* **10**, 955–974 (2011).
- [22] M. Gullans, T. G. Tiecke, D. E. Chang, J. Feist, J. D. Thompson, J. I. Cirac, P. Zoller, and M. D. Lukin, “Nanoplasmonic Lattices for Ultracold Atoms,” *Physical Review Letters* **109**, 235309+ (2012).
- [23] Y. Wang, T. Tran, P. Surendran, I. Herrera, A. Balcytis, D. Nissen, M. Albrecht, A. Sidorov, and P. Hannaford, “Trapping ultracold atoms in a sub-micron-period triangular magnetic lattice,” *Phys. Rev. A* **96**, 013630 (2017).
- [24] O. Romero-Isart, C. Navau, A. Sanchez, P. Zoller, and J. I. Cirac, “Superconducting Vortex Lattices for Ultracold Atoms,” *Phys. Rev. Lett.* **111**, 145304 (2013).
- [25] W. Yi, A. J. Daley, G. Pupillo, and P. Zoller, “State-dependent, addressable subwavelength lattices with cold atoms,” *New Journal of Physics* **10**, 073015 (2008).
- [26] S. Balik, A. L. Win, M. D. Havey, I. M. Sokolov, and D. V. Kupriyanov, “Near-resonance light scattering from a high-density ultracold atomic  $^{87}\text{Rb}$  gas,” *Phys. Rev. A* **87**, 053817 (2013).
- [27] J. Pellegrino, R. Bourgain, S. Jennewein, Y. R. P. Sortais, A. Browaeys, S. D. Jenkins, and J. Ruostekoski, “Observation of suppression of light scattering induced by dipole-dipole interactions in a cold-atom ensemble,” *Phys. Rev. Lett.* **113**, 133602 (2014).
- [28] Julien Chabé, Mohamed-Taha Rouabah, Louis Bellando, Tom Bienaimé, Nicola Piovella, Romain Bachelard, and Robin Kaiser, “Coherent and incoherent multiple scattering,” *Phys. Rev. A* **89**, 043833 (2014).
- [29] C. C. Kwong, T. Yang, D. Delande, R. Pierrat, and D. Wilkowski, “Cooperative emission of a pulse train in an optically thick scattering medium,” *Phys. Rev. Lett.* **115**, 223601 (2015).
- [30] S. L. Bromley, B. Zhu, M. Bishof, X. Zhang, T. Bothwell, J. Schachenmayer, T. L. Nicholson, R. Kaiser, S. F. Yelin, M. D. Lukin, A. M. Rey, and J. Ye, “Collective atomic scattering and motional effects in a dense coherent medium,” *Nat Commun* **7**, 11039 (2016).
- [31] William Guerin, Michelle O. Araújo, and Robin Kaiser, “Subradiance in a large cloud of cold atoms,” *Phys. Rev. Lett.* **116**, 083601 (2016).
- [32] P. C. Bons, R. de Haas, D. de Jong, A. Groot, and P. van der Straten, “Quantum enhancement of the index of refraction in a Bose-Einstein condensate,” *Phys. Rev. Lett.* **116**, 173602 (2016).

- [33] J. Keaveney, A. Sargsyan, U. Krohn, I. G. Hughes, D. Sarkisyan, and C. S. Adams, “Cooperative Lamb shift in an atomic vapor layer of nanometer thickness,” *Phys. Rev. Lett.* **108**, 173601 (2012).
- [34] S. D. Jenkins, J. Ruostekoski, J. Javanainen, R. Bourgain, S. Jennewein, Y. R. P. Sortais, and A. Browaeys, “Optical resonance shifts in the fluorescence of thermal and cold atomic gases,” *Phys. Rev. Lett.* **116**, 183601 (2016).
- [35] S. Jennewein, M. Besbes, N. J. Schilder, S. D. Jenkins, C. Sauvan, J. Ruostekoski, J.-J. Greffet, Y. R. P. Sortais, and A. Browaeys, “Coherent scattering of near-resonant light by a dense microscopic cold atomic cloud,” *Phys. Rev. Lett.* **116**, 233601 (2016).
- [36] L. Corman, J. L. Ville, R. Saint-Jalm, M. Aidelsburger, T. Bienaimé, S. Nascimbène, J. Dalibard, and J. Beugnon, “Transmission of near-resonant light through a dense slab of cold atoms,” *Phys. Rev. A* **96**, 053629 (2017).
- [37] Juha Javanainen, Janne Ruostekoski, Yi Li, and Sung-Mi Yoo, “Shifts of a resonance line in a dense atomic sample,” *Phys. Rev. Lett.* **112**, 113603 (2014).
- [38] Juha Javanainen and Janne Ruostekoski, “Light propagation beyond the mean-field theory of standard optics,” *Opt. Express* **24**, 993–1001 (2016).
- [39] Mark Keil, Omer Amit, Shuyu Zhou, David Groswasser, Yonathan Japha, and Ron Folman, “Fifteen years of cold matter on the atom chip: promise, realizations, and prospects,” *Journal of Modern Optics* **63**, 1840–1885 (2016), <http://dx.doi.org/10.1080/09500340.2016.1178820>.
- [40] V. Y. F. Leung, D. R. M. Pijn, H. Schlatter, L. Torralbo-Campo, A. L. La Rooij, G. B. Mulder, J. Naber, M. L. Soudijn, A. Tauschinsky, C. Abarbanel, B. Hadad, E. Golan, R. Folman, and R. J. C. Spreeuw, “Magnetic-film atom chip with 10  $\mu\text{m}$  period lattices of microtraps for quantum information science with Rydberg atoms,” *Review of Scientific Instruments* **85**, 053102+ (2014).
- [41] S. Whitlock, R. Gerritsma, T. Fernholz, and R. J. C. Spreeuw, “Two-dimensional array of microtraps with atomic shift register on a chip,” *New Journal of Physics* **11**, 023021 (2009).
- [42] Mark D. Lee, Stewart D. Jenkins, and Janne Ruostekoski, “Stochastic methods for light propagation and recurrent scattering in saturated and nonsaturated atomic ensembles,” *Phys. Rev. A* **93**, 063803 (2016).
- [43] See Supplemental Material for additional details regarding technical background information, which includes Refs. [42, 45, 49–51].
- [44] Julian B Naber, Jannie Vos, Robert J Rengelink, Rosanne J Nusselder, and David Davtyan, “Optical techniques for Rydberg physics in lattice geometries A technical guide,” *European Physical Journal-Special Topics* **225**, 2785–2816 (2016).
- [45] Juha Javanainen, Janne Ruostekoski, Bjarne Vestergaard, and Matthew R. Francis, “One-dimensional modelling of light propagation in dense and degenerate samples,” *Phys. Rev. A* **59**, 649–666 (1999).
- [46] Ryan Jones, Reece Saint, and Beatriz Olmos, “Far-field resonance fluorescence from a dipole-interacting laser-driven cold atomic gas,” *Journal of Physics B: Atomic, Molecular and Optical Physics* **50**, 014004 (2017).
- [47] R. T. Sutherland and F. Robicheaux, “Degenerate zee-man ground states in the single-excitation regime,” *Phys. Rev. A* **96**, 053840 (2017).
- [48] Mark D. Lee, Stewart D. Jenkins, Yael Bronstein, and Janne Ruostekoski, “Stochastic electrodynamics simulations for collective atom response in optical cavities,” *Phys. Rev. A* **96**, 023855 (2017).
- [49] John David Jackson, *Classical Electrodynamics*, 3rd ed. (Wiley, New York, 1999).
- [50] Stewart D. Jenkins and Janne Ruostekoski, “Controlled manipulation of light by cooperative response of atoms in an optical lattice,” *Phys. Rev. A* **86**, 031602 (2012).
- [51] C. F. Ockeloen, A. F. Tauschinsky, R. J. C. Spreeuw, and S. Whitlock, “Detection of small atom numbers through image processing,” *Phys. Rev. A* **82**, 061606 (2010).

**SUPPLEMENTAL MATERIAL: COLLECTIVE  
SUPPRESSION OF OPTICAL HYPERFINE  
PUMPING IN DENSE CLOUDS OF ATOMS IN  
MICROTRAPS**

In this Supplemental material we provide a more detailed description of the numerical simulation methods that are used to demonstrate the density-dependent suppression of optical pumping. We also explain the image analysis we perform, and how we convert the optical density image to number of atoms.

**SIMULATION DETAILS**

In the experiment the atoms are confined in an array of microtraps and occupy the  $(5S_{1/2}) |F, m_F\rangle = |2, 2\rangle$  electronic ground state. An incident laser excites the atoms to the  $(5P_{3/2}) |F', m_{F'}\rangle = |2, 1\rangle$  state from which the atoms decay to either the  $F = 2$  manifold, with  $m_F = 0, 1, 2$ , or to non-trapped states in the  $F = 1$  manifold, with  $m_F = 0, 1$ . Reabsorption of light can take the atom to additional levels in the  $F = 1, 2$  and  $F' = 2$  manifolds. The optical pumping rate is measured by detecting the remaining trapped atoms in the  $F = 2$  states.

Standard coupled-dipole model simulations [45] are formulated for a single electronic ground level and for the limit of low light intensity where the atoms respond to light as linear harmonic oscillators. The system we are studying involves more than one electronic ground level that participate in optical transitions and the optical pumping necessitates simulation approaches that go beyond the low light intensity limit, incorporating also the excited state dynamics. In order to do this we apply a recently proposed formalism [42] of coupled-dipole model equations that specifically account for the internal level dynamics. This leads to the stochastic electrodynamics of radiatively coupled equations of motion for each atom. We integrate the dynamics within a semiclassical approximation where quantum correlations between the internal atomic levels are ignored, but where recurrent scattering of light between the different atoms and the resulting spatial correlations due to resonant dipole-dipole interactions are included. The methodology is detailed in Ref. [42].

The procedure for solving for the optical response of the stochastic electrodynamics of light and atoms amounts to a Monte Carlo integration. In each stochastic realization the discrete atomic positions  $\{\mathbf{X}_1, \dots, \mathbf{X}_N\}$  are randomly sampled from the appropriate spatial distribution. For each such a realization, we solve the coupled electrodynamics for light and pointlike atoms at fixed positions. The optical response of the ensemble is then given by averaging quantities of interest over many realizations.

We introduce a notation where  $\hat{\rho}_{ab}(\mathbf{r})$  denotes a single

particle density matrix with  $a, b = e, g$  referring to the electronically excited  $e$  and ground  $g$  levels, where  $e$  and  $g$  also run over the different Zeeman sublevels, and  $\hat{\rho}_{ab}(\mathbf{r})$  corresponds to the annihilation of an atom in the level  $b$  and the creation of an atom in the level  $a$ . We then write  $\hat{\rho}_{ab}(\mathbf{r})$  for  $N$  atoms at fixed positions  $\{\mathbf{X}_1, \dots, \mathbf{X}_N\}$  (corresponding to one particular stochastic realization) as the sum over the atoms  $j$ ,

$$\langle \hat{\rho}_{ab}(\mathbf{r}) \rangle_{\{\mathbf{X}_1, \dots, \mathbf{X}_N\}} = \sum_j \rho_{ab}^{(j)} \delta(\mathbf{r} - \mathbf{X}_j). \quad (2)$$

Then, e.g., the dipole amplitude for the transition  $|g\rangle \leftrightarrow |e\rangle$  is given by

$$\mathbf{d}_{ge}^{(j)} \rho_{ge}^{(j)}(t) = \mathcal{D} \sum_{\sigma=-1}^1 \mathcal{C}_{g,e}^{(\sigma)} \hat{\mathbf{e}}_{\sigma} \rho_{ge}^{(j)}(t), \quad (3)$$

and the corresponding positive frequency component of the atomic polarization density

$$\langle \hat{\mathbf{P}}^+ \rangle_{\{\mathbf{X}_1, \dots, \mathbf{X}_N\}} = \sum_j \sum_{ge} \mathbf{d}_{ge}^{(j)} \rho_{ge}^{(j)}(t) \delta(\mathbf{r} - \mathbf{X}_j), \quad (4)$$

where  $\mathcal{C}_{g,e}^{(\sigma)} \equiv \langle 1F_g; F_e e | F_g g; 1\sigma \rangle$  are Clebsch-Gordan coefficients for the corresponding dipole transition ( $F_f$  is the total atomic angular momentum of hyperfine level  $f$ ),  $\mathcal{D}$  is the reduced dipole matrix element, and  $\sigma = -1, 0, 1$  is an index indicating the unit circular polarization vectors.

Here and elsewhere in this paper we have assumed that the atoms are illuminated by an incident laser with the dominant frequency  $\Omega$ , and that all the relevant quantities are expressed as slowly varying amplitudes by explicitly factoring out the laser frequency oscillations by writing  $\hat{\mathbf{P}}^+ \rightarrow e^{-i\Omega t} \hat{\mathbf{P}}^+$ , and similarly for electric displacement  $\mathbf{D}^+ \rightarrow e^{-i\Omega t} \mathbf{D}^+$  and electric field  $\mathbf{E}^+ \rightarrow e^{-i\Omega t} \mathbf{E}^+$ .

The electric field amplitude may be expressed as the sum of the incident and the scattered fields

$$\epsilon_0 \mathbf{E}^+(\mathbf{r}) = \mathbf{D}_F^+(\mathbf{r}) + \int d^3r' \mathbf{G}(\mathbf{r} - \mathbf{r}') \mathbf{P}^+(\mathbf{r}'), \quad (5)$$

where the monochromatic dipole radiation kernel [49]  $\mathbf{G}(\mathbf{r})$  provides the radiated field at  $\mathbf{r}$  from a dipole with the amplitude  $\hat{\mathbf{d}}$  residing at the origin ( $k = \Omega/c$ ):

$$\mathbf{G}(\mathbf{r}) \hat{\mathbf{d}} = \frac{k^3}{4\pi} \left\{ (\hat{\mathbf{n}} \times \hat{\mathbf{d}}) \times \hat{\mathbf{n}} \frac{e^{ikr}}{kr} + [3\hat{\mathbf{n}}(\hat{\mathbf{n}} \cdot \hat{\mathbf{d}}) - \hat{\mathbf{d}}] \left[ \frac{1}{(kr)^3} - \frac{i}{(kr)^2} \right] e^{ikr} \right\} - \frac{\hat{\mathbf{d}} \delta(\mathbf{r})}{3}, \quad (6)$$

where  $\hat{\mathbf{n}} = \mathbf{r}/r$ .

The light mediates strong interactions between the atoms. Each atom is driven by the incident field and the field scattered by all the other atoms in the ensemble.

ble. This yields the coupled equations of motion for  $\rho_{ab}^{(j)}$  for each atom  $j$  and internal levels  $a, b$ .

We introduce an abbreviated notation for the radiative coupling coefficients between the atoms at the locations  $\mathbf{X}_j$  and  $\mathbf{X}_l$  as  $\mathcal{G}_{\sigma\zeta}^{(jl)}$  that mediate the interactions between dipoles of orientations  $\hat{\mathbf{e}}_\sigma$  and  $\hat{\mathbf{e}}_\zeta$ ,

$$\mathcal{G}_{\sigma\zeta}^{(jl)} = \hat{\mathbf{e}}_\sigma^* \cdot \mathbf{G}(\mathbf{X}_j - \mathbf{X}_l) \hat{\mathbf{e}}_\zeta. \quad (7)$$

We can then derive the equations of motion for the atomic level density matrix elements for each atom  $j$  in the ensemble to correspond to the experimental system with one electronically excited level  $e$ , where the indices  $g$  run over all the electronic ground states in the system

$$\begin{aligned} \frac{d}{dt} \rho_{ge}^{(j)} &= (i\Delta_{ge} - \Gamma) \rho_{ge}^{(j)} + i \frac{\xi}{\mathcal{D}} \rho_{gg'}^{(j)} \mathcal{C}_{g',e}^{(\sigma)} \hat{\mathbf{e}}_\sigma^* \cdot \mathbf{D}_F^+(\mathbf{X}_j) \\ &\quad - i \frac{\xi}{\mathcal{D}} \rho_{ee}^{(j)} \mathcal{C}_{g,e}^{(\sigma)} \hat{\mathbf{e}}_\sigma^* \cdot \mathbf{D}_F^+(\mathbf{X}_j) \\ &\quad + i \xi \sum_{l \neq j} \mathcal{C}_{g',e}^{(\sigma)} \mathcal{G}_{\sigma\zeta}^{(jl)} \mathcal{C}_{g'',e}^{(\zeta)} \rho_{g''e}^{(l)} \rho_{gg'}^{(j)} \\ &\quad - i \xi \sum_{l \neq j} \mathcal{C}_{g,e}^{(\sigma)} \mathcal{G}_{\sigma\zeta}^{(jl)} \mathcal{C}_{g'',e}^{(\zeta)} \rho_{g''e}^{(l)} \rho_{ee}^{(j)}, \end{aligned} \quad (8a)$$

$$\begin{aligned} \frac{d}{dt} \rho_{gg'}^{(j)} &= i\Delta_{gg'} \rho_{gg'}^{(j)} + 2\Gamma \mathcal{C}_{g',e}^{(\sigma)} \mathcal{C}_{g,e}^{(\sigma)} \rho_{ee}^{(j)} \\ &\quad - i \frac{\xi}{\mathcal{D}} \rho_{eg}^{(j)} \mathcal{C}_{g,e}^{(\sigma)} \hat{\mathbf{e}}_\sigma^* \cdot \mathbf{D}_F^+(\mathbf{X}_j) + i \frac{\xi}{\mathcal{D}} \rho_{ge}^{(j)} \mathcal{C}_{g',e}^{(\sigma)} \hat{\mathbf{e}}_\sigma \cdot \mathbf{D}_F^-(\mathbf{X}_j) \\ &\quad - i \xi \sum_{l \neq j} \mathcal{C}_{g,e}^{(\sigma)} \mathcal{G}_{\sigma\zeta}^{(jl)} \mathcal{C}_{g'',e}^{(\zeta)} \rho_{g''e}^{(l)} \rho_{eg'}^{(j)} \\ &\quad + i \xi \sum_{l \neq j} \mathcal{C}_{g',e}^{(\sigma)} [\mathcal{G}_{\sigma\zeta}^{(jl)}]^* \mathcal{C}_{g'',e}^{(\zeta)} \rho_{g''e}^{(l)} \rho_{ge}^{(j)}, \end{aligned} \quad (8b)$$

$$\begin{aligned} \frac{d}{dt} \rho_{ee}^{(j)} &= -2\Gamma \rho_{ee}^{(j)} - 2\text{Im} \left[ \frac{\xi}{\mathcal{D}} \rho_{eg}^{(j)} \mathcal{C}_{g,e}^{(\sigma)} \hat{\mathbf{e}}_\sigma^* \cdot \mathbf{D}_F^+(\mathbf{X}_j) \right] \\ &\quad - 2\text{Im} \left[ \xi \sum_{l \neq j} \mathcal{C}_{g,e}^{(\sigma)} \mathcal{G}_{\sigma\zeta}^{(jl)} \mathcal{C}_{g'',e}^{(\zeta)} \rho_{g''e}^{(l)} \rho_{eg}^{(j)} \right]. \end{aligned} \quad (8c)$$

Here the repeated indices  $\sigma, \zeta$  and the ground state symbols that do not appear on the left-hand-side are implicitly summed over,  $\xi = \mathcal{D}^2/(\hbar\epsilon_0)$ , and the detuning of the incident light from the atomic resonances is given by  $\Delta_{ge} = \Omega - \omega_{ge}$ . In the case of a conserved total atom population, one of the equations can be eliminated by the relation  $\sum_g \rho_{gg}^{(j)} + \sum_e \rho_{ee}^{(j)} = 1$ . We have introduced a semiclassical approximation to factorize internal level two-body correlation functions. Due to this approximation, the ensemble average of many single realizations does not reproduce the nonclassical correlations in the system.

Instead of considering the full experimental configuration of all the  $F = 1, 2$  and  $F' = 2$  electronic levels, we approximate the system in the numerical simulations

by an effective three-level model where one of the ground levels refers to the initial state  $|1\rangle \equiv |F, m_F\rangle = |2, 2\rangle$ , and all the final electronic ground levels are approximated by a single state  $|2\rangle$ . Resonant incident light then drives the transition  $|1\rangle \leftrightarrow |e\rangle$  to an electronically excited state  $|e\rangle$ , and the atoms can spontaneously decay to both levels  $|1\rangle$  and  $|2\rangle$ . For instance, when the transition strengths are equal for the two levels (and the atom can only decay for the two ground levels studied), the equations of motion then simplify to

$$\begin{aligned} \frac{d}{dt} \rho_{1e}^{(j)} &= (i\Delta_{1e} - \Gamma) \rho_{1e}^{(j)} + i \frac{\xi}{\sqrt{2}\mathcal{D}} \rho_{11}^{(j)} \hat{\mathbf{e}}_1^* \cdot \mathbf{D}_F^+(\mathbf{X}_j) \\ &\quad - i \frac{\xi}{\sqrt{2}\mathcal{D}} \rho_{ee}^{(j)} \hat{\mathbf{e}}_1^* \cdot \mathbf{D}_F^+(\mathbf{X}_j) + i \frac{\xi}{2} \sum_{l \neq j} \mathcal{G}_{g'g}^{(jl)} \rho_{ge}^{(l)} \rho_{1g'}^{(j)} \\ &\quad - i \frac{\xi}{2} \sum_{l \neq j} \mathcal{G}_{1g}^{(jl)} \rho_{ge}^{(l)} \rho_{ee}^{(j)}, \end{aligned} \quad (9a)$$

$$\begin{aligned} \frac{d}{dt} \rho_{2e}^{(j)} &= (i\Delta_{2e} - \Gamma) \rho_{2e}^{(j)} + i \frac{\xi}{\sqrt{2}\mathcal{D}} \rho_{21}^{(j)} \hat{\mathbf{e}}_1^* \cdot \mathbf{D}_F^+(\mathbf{X}_j) \\ &\quad + i \frac{\xi}{2} \sum_{l \neq j} \mathcal{G}_{g'g}^{(jl)} \rho_{ge}^{(l)} \rho_{2g'}^{(j)} - i \frac{\xi}{2} \sum_{l \neq j} \mathcal{G}_{2g}^{(jl)} \rho_{ge}^{(l)} \rho_{ee}^{(j)}, \end{aligned} \quad (9b)$$

$$\begin{aligned} \frac{d}{dt} \rho_{12}^{(j)} &= i\Delta_{12} \rho_{12}^{(j)} + \Gamma \rho_{ee}^{(j)} - i \frac{\xi}{\sqrt{2}\mathcal{D}} \rho_{e2}^{(j)} \hat{\mathbf{e}}_1^* \cdot \mathbf{D}_F^+(\mathbf{X}_j) \\ &\quad - i \frac{\xi}{2} \sum_{l \neq j} \mathcal{G}_{1g}^{(jl)} \rho_{ge}^{(l)} \rho_{e2}^{(j)} + i \frac{\xi}{2} \sum_{l \neq j} [\mathcal{G}_{2g}^{(jl)}]^* \rho_{eg}^{(l)} \rho_{1e}^{(j)}, \end{aligned} \quad (9c)$$

$$\begin{aligned} \frac{d}{dt} \rho_{11}^{(j)} &= +\Gamma \rho_{ee}^{(j)} + \sqrt{2}\text{Im} \left[ \frac{\xi}{\mathcal{D}} \rho_{e1}^{(j)} \hat{\mathbf{e}}_1^* \cdot \mathbf{D}_F^+(\mathbf{X}_j) \right] \\ &\quad + \text{Im} \left[ \xi \sum_{l \neq j} \mathcal{G}_{1g}^{(jl)} \rho_{ge}^{(l)} \rho_{e1}^{(j)} \right], \end{aligned} \quad (9d)$$

$$\frac{d}{dt} \rho_{22}^{(j)} = +\Gamma \rho_{ee}^{(j)} + \text{Im} \left[ \xi \sum_{l \neq j} \mathcal{G}_{2g}^{(jl)} \rho_{ge}^{(l)} \rho_{e2}^{(j)} \right], \quad (9e)$$

$$\begin{aligned} \frac{d}{dt} \rho_{ee}^{(j)} &= -2\Gamma \rho_{ee}^{(j)} - \sqrt{2}\text{Im} \left[ \frac{\xi}{\mathcal{D}} \rho_{e1}^{(j)} \hat{\mathbf{e}}_1^* \cdot \mathbf{D}_F^+(\mathbf{X}_j) \right] \\ &\quad - \text{Im} \left[ \xi \sum_{l \neq j} \mathcal{G}_{gg'}^{(jl)} \rho_{g'e}^{(l)} \rho_{eg}^{(j)} \right], \end{aligned} \quad (9f)$$

where the ground state symbols are again summed over.

The result is a set of coupled equations (9) for internal level one-body density matrix elements  $\rho_{ab}^{(j)}$ , for each atom  $j = 1, \dots, N$ . In the absence of the radiative coupling terms  $\mathcal{G}_{gg'}^{(jl)}$ , with  $g, g' = 1, 2$  the equations coincide with standard Bloch equations. The terms  $\mathcal{G}_{gg'}^{(jl)}$  represent the strong resonant dipole-dipole interactions that depend on the relative positions between the atoms and

TABLE I. Simulated atom numbers for each trap radius and the corresponding peak atom densities.

$r$	$N$	$10^{-3}\rho/k^3$
1	12, 18, 25, 35	18, 27, 38, 53
$\sqrt{2}$	8, 12, 15	34, 51, 63
$1.7\sqrt{2}$	3, 6, 9	62, 120, 190
$2.5\sqrt{2}$	3, 4, 5, 7	200, 270, 330, 470

lead to spatial correlations in the optical response. In the limit that the resonance frequencies of the different transitions differ considerably, the cross terms  $\mathcal{G}_{gg'}^{(jl)}$ , with  $g \neq g'$  – that couple the different transitions  $|1\rangle \leftrightarrow |e\rangle$  and  $|2\rangle \leftrightarrow |e\rangle$  – become negligible. The standard two-level coupled dipole model approach [45, 50] is obtained from Eq. (9b) by setting all the terms involving  $\rho_{ee}$  to zero and the indices  $g = g' = 1$ .

In the simulations, we then stochastically sample the set of discrete atomic coordinates  $\{\mathbf{X}_1, \dots, \mathbf{X}_N\}$  from the density distribution. For each realization we solve the semiclassical electrodynamics equations of motion (9) for all  $\rho_{ab}^{(j)}$ . Averaging over many such realizations allows the expectation values of desired observables to be computed. The simulations then incorporate all the recurrent scattering events between the atoms in a semi-classical approximation for random positions of the atoms.

## SIMULATION RESULTS

We simulate the remaining population in the initial state  $\rho_{11}$  as a function of time that yields exponential decay rates (calculated from the initial population and the  $t = 500/\Gamma$  results). These rates are called pumping rates, each of which is represented by a single data point in Fig. 4(a) of the main text. The different data sets in Fig. 4 are obtained for different cloud radii, resulting in the variation of both the atom density and optical thickness. Table I shows the simulated atom numbers for atom clouds whose radius is smaller by the factor  $r$  than the experimental value (the aspect ratios are the same in all cases).

## NUMBER OF ATOMS CALCULATION

In this experiment we use absorption imaging in order to measure the optical thickness of the atomic clouds. The optical thickness is then converted to number of atoms per pixel. This conversion depends on the camera pixel size, the magnification, and the absorption cross section  $\sigma$ . Our camera’s pixel size and magnification are known (13  $\mu\text{m}$  and 13, respectively), but  $\sigma$  should be sim-

ulated. For an imaging laser with  $\sigma^+$  polarization driving the  $|2, 2\rangle \rightarrow |3, 3\rangle$  transition  $\sigma_0 = 3\lambda^2/2\pi$ . In our system, however, the initial state is a distribution over the  $m_F$  states of the  $F = 2$  ground state, and the imaging polarization is  $\pi$ . In addition, the atomic distribution in the ground state changes during the imaging pulse. In order to find the effective cross section  $\sigma_{\text{eff}}$  (time averaged over the imaging pulse) we solve the optical Bloch equations (OBE) for the 12 relevant states (5 Zeeman sublevels of the  $F = 2$  ground state, and 7 for the  $F' = 3$  excited state) using our experimental parameters ( $s = 0.05$  and  $B = 5.4$  G) with different initial conditions (initial distribution). We find that

$$\sigma_{\text{eff}} = (0.15 \pm 0.02)\sigma_0. \quad (10)$$

The error in  $\sigma_{\text{eff}}$  is due to the different initial distributions, and it is the main contribution to the error bars in number of atoms in the figures (the other source of error is shot-to-shot fluctuations). We would like to note that  $\sigma_{\text{eff}}$  includes a factor 0.5 to compensate the retro-reflecting imaging scheme we use.

In order to improve our image quality and lower the noise in the image and the number of atoms we use two more algorithms: fringe removal and deconvolution. The fringe removal algorithm [51] takes an array of images of the imaging laser with no atomic cloud and generates a new image, which is a linear combination of these images, that minimizes the fringe visibility in the optical density image. This minimization is done in an area with no atoms, and the linear combination has different weights for each measurement. This algorithm deals with the main noise contribution that comes from fringes due to spurious reflections, which does not cancel well in the optical density image. It assumes that if these fringes will be canceled in the area near the atoms, this cancellation will be valid also in the area with atoms.

The second algorithm, the deconvolution, is performed because signal from one microtrap ‘leaks’ to neighboring sites. This leakage is a convolution of the ‘real’ number of atoms with a point-spread-function (PSF). Using a second order correlation matrix  $g^{(2)}$  we confirm that the signal in each trap depends on its neighboring sites. We also find, using a fitting algorithm, a PSF that creates the same dependence of a site on its neighbors (the correlation matrix). The last step is to deconvolute our images with the fitted PSF. We would like to note that here we do not use the single pixels of the CCD. We rather sum a square around each microtrap [the square in Fig. 5] and use it as a ‘pixel’ for the deconvolution algorithm. The deconvoluted number of atoms is presented in figures 2 and 3 in the main text of the paper.

## MICROTRAPS GROUPS

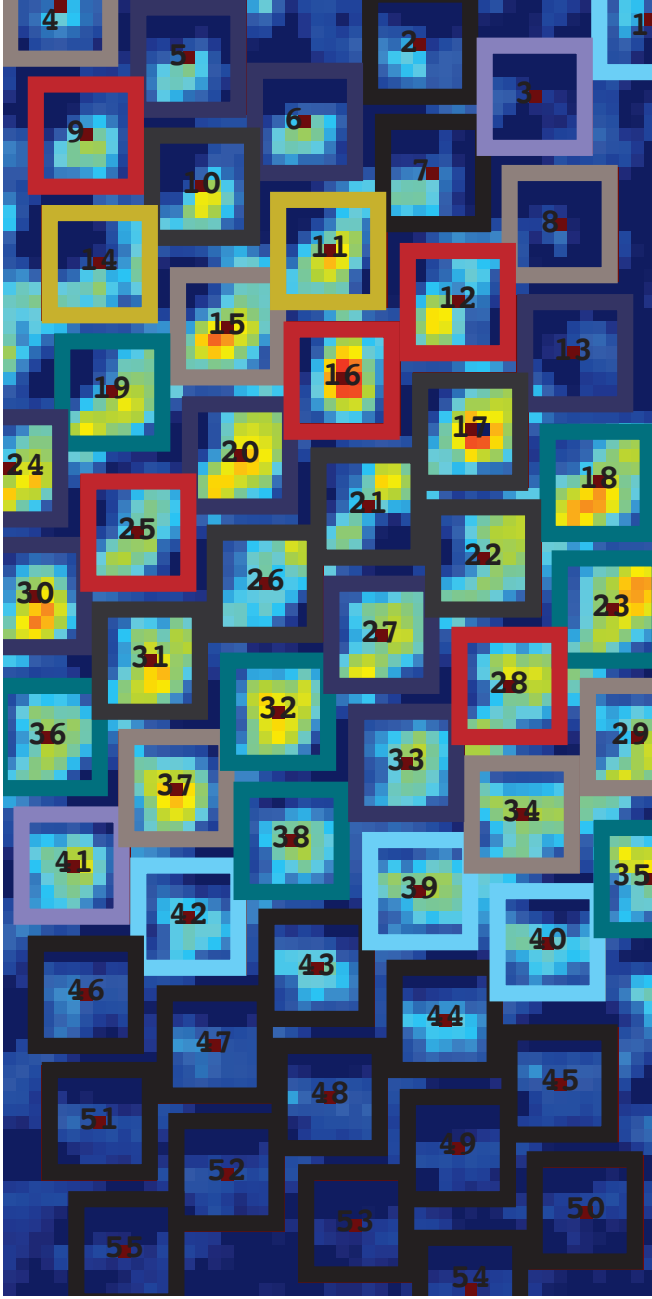


FIG. 5. The analysis area. Each microtrap center is marked with a red dot and a site index. The squares around the microtraps represent the area where we count the atoms, and the colors indicate the groups (see Table II). Traps that appear to be cut still use a full-size square to count the number of atoms by counting the relevant area outside the image shown here.

The analysis in this work was not done on a single cloud level, but rather on groups of clouds. This was done in order to reduce noise. The grouping was done based on the initial number of atoms in each site, which

TABLE II. Grouping of microtraps based on initial number of atoms.

	site index	$N_0$
group 1	1, 39, 40, 42	$33 \pm 5$
group 2	3, 41	$58 \pm 8$
group 3	4, 8, 15, 29, 34, 37	$84 \pm 11$
group 4	18, 19, 23, 32, 35, 36, 38	$103 \pm 14$
group 5	5, 6, 20, 24, 27, 30	$131 \pm 18$
group 6	10, 13, 33	$157 \pm 21$
group 7	17, 21, 22, 26, 31	$181 \pm 24$
group 8	9, 12, 16, 25, 28	$204 \pm 27$
group 9	11, 14	$232 \pm 31$

is averaged over 26 images. Figure 5 shows the area where we perform our analysis, and the individual microtraps. The pumping time is zero in the figure, and it shows the initial microtraps densities. The color of the square indicates the group, see Table II for site indexes for each group. The sites marked with black squares are ignored because of low atom number.